

# Record-High Gain and Detectivity in Unipolar Barrier Solar Blind Avalanche Photodetector *via* Deliberate Lattice and Band Engineering

**Qingyi Zhang**

Beijing University of Posts and Telecommunications

**Ning Li**

Beijing University of Posts and Telecommunications

**Tao Zhang**

Beijing University of Posts and Telecommunications

**Dianmeng Dong**

Beijing University of Posts and Telecommunications

**Yongtao Yang**

Beijing University of Posts and Telecommunications

**Yuehui Wang**

Beijing University of Posts and Telecommunications <https://orcid.org/0000-0002-7902-2813>

**Zhengang Dong**

Beijing University of Posts and Telecommunications

**Jiaying Shen**

Beijing University of Posts and Telecommunications

**Tianhong Zhou**

Nankai University

**Yuanlin Liang**

Nankai University

**Weihua Tang**

Beijing University of Posts and Telecommunications

**Yang Zhang**

Nankai University

**Zhenping Wu**

Beijing University of Posts and Telecommunications <https://orcid.org/0000-0003-2986-8068>

**Jianhua Hao** (✉ [jh.hao@polyu.edu.hk](mailto:jh.hao@polyu.edu.hk))

The Hong Kong Polytechnic University <https://orcid.org/0000-0002-6186-5169>

---

**Article**

**Keywords:**

**Posted Date:** June 14th, 2022

**DOI:** <https://doi.org/10.21203/rs.3.rs-1737382/v1>

**License:** © ⓘ This work is licensed under a Creative Commons Attribution 4.0 International License. [Read Full License](#)

---

**Version of Record:** A version of this preprint was published at Nature Communications on January 26th, 2023. See the published version at <https://doi.org/10.1038/s41467-023-36117-8>.

# Abstract

Ga<sub>2</sub>O<sub>3</sub>-based solar blind avalanche photodetectors (APDs) allow low voltage operation, optical filter-free and monolithic integration of PD arrays, and therefore they are promising to be alternative to the bulky and fragile photomultiplier tube (PMT) in weak deep-ultraviolet signal detection. However, so far the performances of all reported Ga<sub>2</sub>O<sub>3</sub>-based APDs are still inferior to PMTs due to restricted breakdown electric field and monolithic integration limitations. Here, by deliberate lattice and band engineering, we construct an n-Barrier-n (nBn) unipolar barrier APD consisting of  $\beta$ -Ga<sub>2</sub>O<sub>3</sub>/MgO/Nb:STO heterostructure, in which the enlarged conduction band offsets fortify the reverse breakdown and suppress the dark current while the negligible valance band offsets facilitate minority carrier flow. The lattice and band engineered unipolar barrier configuration provides deterministic control over the charge carriers flow and related avalanche multiplication effects. The developed unipolar barrier APDs exhibit record-high avalanche gain up to  $5.86 \times 10^5$  and detectivity of  $3.28 \times 10^{17}$  Jones among the wafer-scale grown Ga<sub>2</sub>O<sub>3</sub>-based PDs, which are even comparable with commercial PMTs. These findings provide new insights into precise control of band alignment in APDs, which also offer great opportunities for high-performance Ga<sub>2</sub>O<sub>3</sub>-based electronics and optoelectronics.

## 1. Introduction

Solar blind photodetectors (PDs) enable photoelectric transduction within the wavelengths of 200 ~ 280 nm. They generate electrical signals solely responded to deep-ultraviolet (DUV) light, with particular applications ranging from security communication to missile or fire alarms detections<sup>1-3</sup>. To date, solar blind detection for both civilian and military applications has been mainly accomplished by photomultiplier tubes (PMTs) based on the non-thermionic vacuum tubes made of glass, which are favored in weak UV signal sensing resorting to their ultrahigh internal gain ( $\sim 10^6$ )<sup>4,5</sup>. However, PMTs operate at high voltage above 1 kV and need external Wood's optical filters to eliminate the longer wavelength light influence, the attendant bulky power sources with strict requirement of high stability, evacuated glass construction, magnetic shielding requested in some circumstance and fragile optical filter. Putting all these limitations of PMTs together, it is imperative to explore alternatives to PMTs and all-solid state PDs are ideal candidate in principle by considering future monolithic integration possibility. Wide-bandgap semiconductors such as AlGa<sub>n</sub>, MgZnO, and Ga<sub>2</sub>O<sub>3</sub> have sprung to the forefront of solar blind detection activity owing to their key attributes, such as intrinsic solar-rejection, high breakdown electric field, chemical and thermal stability<sup>6-8</sup>. On contrast to PMTs, wide-bandgap semiconductor-based solar blind PDs may enjoy the features of low voltage operation and optical filter-free integration, and promise more compact and robust monolithic integration of PD arrays. To meet the requirements of the cutoff wavelength of 280 nm, alloying engineering is necessary for high Al/Mg contents AlGa<sub>n</sub> and MgZnO. Unfortunately, owing to the high growth temperature (> 1350°C) for AlGa<sub>n</sub> and wurtzite-rocksalt phase segregation in MgZnO, plenty of defects/dislocations are occurred in ternary semiconductor AlGa<sub>n</sub> and MgZnO films, inevitably degrading the relevant devices' performances<sup>9,10</sup>. Inspiringly, Ga<sub>2</sub>O<sub>3</sub> with a suitable bandgap ( $\sim 4.9$  eV) has been recognized as an excellent candidate suitable for promoting solar blind PDs<sup>11-14</sup>. In the past decade, Ga<sub>2</sub>O<sub>3</sub>-based solar blind PDs of different architectures and designs have been proposed, including photoconductive PDs<sup>15-17</sup>, Schottky barrier PDs<sup>18,19</sup>, and avalanche PDs (APDs)<sup>20-22</sup>. APDs promise orders of magnitude higher responsivity and gain than other types, and conceivably are becoming the research hotspot of the field<sup>23</sup>. Despite unremitting efforts, the performance metrics for reported avalanche PDs (APDs) including responsivity and avalanche gain still lag behind the benchmark of commercial PMTs. The strategy for further enhancing the detectivity and internal gain of APDs heavily relies on increasing the reverse bias while blocking the dark current.

Due to the paucity of bipolar doping, and the complexity of heterojunction formation, only a handful of high-gain Ga<sub>2</sub>O<sub>3</sub>-based APDs have been proposed based on n-n isotype architecture<sup>20-22</sup>. Nevertheless, the conduction band offsets ( $\Delta E_C$ ) are limited by the difference between the electron affinity  $\chi_s$  of the constitutive n-type semiconductors. Further improvement in internal gain can be achieved by constructing Ga<sub>2</sub>O<sub>3</sub>-based heterojunctions with enlarged barrier height, or rather the  $\Delta E_C$ . Modification of the barrier height has been carried out by insertion of a wide bandgap insulator barrier to form an n-Barrier-n (nBn) heterostructure, in which the enlarged band offsets fortify the reverse breakdown and suppress the dark current.<sup>24,25</sup> On further analysis, APDs with an nBn unipolar barrier design can significantly improve the performance of solar blind PDs. For Ga<sub>2</sub>O<sub>3</sub>-based APDs upon

UV irradiation, photon-induced electrons and holes are accelerated and undergo cascade amplifications through impact ionization with increasing the reverse bias. An appealing feature of unipolar barrier design is that a nearly zero valence band offset ( $\Delta E_V$ ) allows the generated holes to flow through the barrier unimpededly, rather than accumulate at the interface occurred in conventional bipolar barrier structure. Unipolar barrier construction, however, suffers from the strict limitations associated with lattice and band matching. To date, unipolar barrier PDs have only been investigated in the visible and infrared region<sup>24-27</sup>.

The advent in synthesizing high-quality epitaxial Ga<sub>2</sub>O<sub>3</sub> on oxides provides enticing opportunities to build an nBn unipolar barrier APDs with dramatically enhanced performance. Here, we construct unipolar barrier solar blind APDs consisting of  $\beta$ -Ga<sub>2</sub>O<sub>3</sub>/MgO/Nb:STO heterostructures. The deliberately designed heterostructure possesses the  $\Delta E_C$  between  $\beta$ -Ga<sub>2</sub>O<sub>3</sub>/MgO and MgO/Nb:STO estimated up to 3.01 eV and 4.18 eV, respectively plus a near zero valence band offset  $\Delta E_V$  formed at the interfaces. The proposed unipolar barrier APDs exhibit recording-high gain and ultrahigh detectivity among the wafer-scale grown Ga<sub>2</sub>O<sub>3</sub>-based PDs, which are comparable with commercial PMTs. These findings present an unexploited architecture of unipolar barrier design applied in solar blind APDs, and the proposed strategies have tremendous potential to develop Ga<sub>2</sub>O<sub>3</sub>-based electronics require high breakdown fields.

## 2. Results

**Device fabrication and characterization of epitaxial heterostructures.** To design an effective unipolar barrier APD device, both interfacial lattice compatible and energy band offsets need careful considerations. By taking account of our previous experimental results<sup>28</sup> (Supplementary Fig. S1), MgO was integrated with Ga<sub>2</sub>O<sub>3</sub> to form a unipolar barrier structure possessing a large conduction band offset  $\Delta E_C$  and nearly zero valence band offset  $\Delta E_V$ . We fabricated an nBn unipolar barrier APD based on the as-prepared Ga<sub>2</sub>O<sub>3</sub>/MgO/Nb:STO heterostructure using laser molecular beam epitaxy (LMBE) assisted by *in-situ* reflection high-energy electron diffraction (RHEED) (Fig. 1a, growth details in Methods Section). A Ga<sub>2</sub>O<sub>3</sub>/Nb:STO heterostructure was also fabricated for APD devices performance comparison. The evolution of the RHEED specular spot intensity enables us to monitor the quality and the thickness of both MgO and Ga<sub>2</sub>O<sub>3</sub> layers at atomic scale. Figure 1b shows the typical RHEED patterns for a Ga<sub>2</sub>O<sub>3</sub>/MgO/Nb:STO heterostructure. The streaky RHEED patterns observed at the end of the deposition for both MgO and Ga<sub>2</sub>O<sub>3</sub> layers verify flat interface and surface. Atomic force microscopy (AFM) indeed reveals a surface topography with a root-mean square (rms) roughness values less than 1.3 nm, as shown in Supplementary Fig. S2. Such uniform and well-defined interface could therefore minimize the interfacial defects/dislocations and benefit the carrier flow cross the heterostructure. The thickness of Ga<sub>2</sub>O<sub>3</sub> (200 nm) and MgO (25 nm) layers were confirmed by both ellipsometer and cross-sectional scanning electron microscopy (Fig. 1c). The X-ray diffraction (XRD)  $\theta$ - $2\theta$  scan manifests sharp (100) diffraction peaks of  $\beta$ -Ga<sub>2</sub>O<sub>3</sub> and MgO, indicating that both Ga<sub>2</sub>O<sub>3</sub>/MgO/Nb:STO and Ga<sub>2</sub>O<sub>3</sub>/Nb:STO heterostructures are of epitaxial form (Fig. 1d). And the out-of-plane relationship is  $\beta$ -Ga<sub>2</sub>O<sub>3</sub>[600]//MgO[200]//Nb:STO[200]. Off-specular  $\Phi$ -scan was then conducted to investigate the in-plane film-substrate alignment. As shown in Fig. 1e, the oblique Ga<sub>2</sub>O<sub>3</sub> {710}, MgO {220} and Nb:STO {220} Bragg reflections appear at coinciding angles and separated azimuthally by 90°, revealing that the Ga<sub>2</sub>O<sub>3</sub> lattice is rotated by 45° on the MgO (100) surface. Thus, the in-plane relationship of the unipolar heterostructure could be assigned to  $\beta$ -Ga<sub>2</sub>O<sub>3</sub>[001]//MgO[011]//Nb:STO[011]. For monoclinic structured  $\beta$ -Ga<sub>2</sub>O<sub>3</sub>, the oxygen atoms along [010] and [001] directions are arranged approximately as equilateral squares, with spacing of 0.304 nm and 0.29 nm, respectively<sup>29</sup>. On the other hand, the oxygen atoms spacing along [011] and [01 $\bar{1}$ ] directions in cubic structured MgO and Nb:STO have the same squared arrangement with spacing of 0.298 nm and 0.276 nm, respectively. Therefore, when the Ga<sub>2</sub>O<sub>3</sub>/MgO/Nb:STO nBn unipolar heterostructure is constructed, Ga atoms in the  $\beta$ -Ga<sub>2</sub>O<sub>3</sub> (100) plane could bond to the oxygen atom layer in the MgO/Nb:STO (100) plane with 45° rotation. A schematic atomic picture of the cross-sectional heterostructure and the interfacial oxygen-atom arrangements are depicted in Fig. 1f and 1g. Thus, the exquisite control offered by the LMBE assisted by *in-situ* Rheed has enabled the direct integration of epitaxial Ga<sub>2</sub>O<sub>3</sub>/MgO heterostructure on Nb:STO.

**Unipolar barrier calculations.** We conducted X-ray photoelectron spectroscopy (XPS) to explore the band diagram of the Ga<sub>2</sub>O<sub>3</sub>/MgO/Nb:STO and the Ga<sub>2</sub>O<sub>3</sub>/Nb:STO heterostructures (Fig. 2a and Supplementary Fig. S3)<sup>30</sup>. According to Kraut's

method, the  $\Delta E_V$  could then be determined by analyzing the binding energy difference between the valence band maximum (VBM) and the core-level shifts (see Method Section)<sup>28</sup>. The obtained  $\Delta E_V$  for the Ga<sub>2</sub>O<sub>3</sub>/Nb:STO is 0.46 eV, while the  $\Delta E_V$  for the Ga<sub>2</sub>O<sub>3</sub>/MgO/Nb:STO are  $\Delta E_{V-Ga_2O_3/MgO} = 0.12$  eV and  $\Delta E_{V-MgO/Nb:STO} = 0.45$  eV, respectively. Then, considering the bandgap ( $E_g$ ) values for Ga<sub>2</sub>O<sub>3</sub> (4.94 eV), MgO (7.83 eV), and Nb:STO (3.2 eV), the calculated conduction-band offset ( $\Delta E_C$ ) for the Ga<sub>2</sub>O<sub>3</sub>/Nb:STO is 1.28 eV. Importantly, the obtained valence band arrangements for Ga<sub>2</sub>O<sub>3</sub>/MgO/Nb:STO are  $\Delta E_{C-Ga_2O_3/MgO} = 3.01$  eV and  $\Delta E_{C-MgO/Nb:STO} = 4.18$  eV, respectively. Therefore, the band diagrams for both the Ga<sub>2</sub>O<sub>3</sub>/MgO/Nb:STO and Ga<sub>2</sub>O<sub>3</sub>/Nb:STO heterostructures in equilibrium condition are illustrated in Fig. 2b and Supplementary **Fig. S4**. The challenging issue for building Ga<sub>2</sub>O<sub>3</sub>-based heterojunctions is the intrinsic large bandgap of Ga<sub>2</sub>O<sub>3</sub>, which limits the selection of dielectrics as the designed barrier. The bandgap of MgO can reach up to 7.83 eV, which is much larger than that of Ga<sub>2</sub>O<sub>3</sub> (4.94 eV), favoring the construction of a rectifying junction with large band offset. More intriguingly, with an elaborate design, the as-prepared nBn-type heterojunction exhibits desired unipolar barrier characteristics, i.e., an extremely high  $\Delta E_C$  and a negligible  $\Delta E_V$  across the Ga<sub>2</sub>O<sub>3</sub>/MgO/Nb:STO heterointerfaces. The carrier transport behaviors of the heterostructures are controlled by the energy band structure. The general purpose of unipolar barrier design is blocking one type of carrier while allowing the flow of the other. In the case of APDs presented here, the large  $\Delta E_C$  can effectively block the electron transfer from Nb:STO to Ga<sub>2</sub>O<sub>3</sub>, which is able to solve the bottleneck of dark current and further improve the performance of APDs. APDs work in a high reverse bias condition and therefore avalanche multiplication is successfully occurred as designed when the excess carriers are formed upon the UV photon impact. The band alignment facilitates the separation and migration of photoexcited carriers. With increasing the reverse bias, photon-induced charge carriers are accelerated and undergo cascade amplifications through impact ionization in the depletion layer. Ionization coefficients of both electrons and holes increase along with the electric field in the depletion region. Therefore, higher reverse voltage generally contribute to higher gain. The large breakdown electric field ( $\sim 8$  MV/cm) endows Ga<sub>2</sub>O<sub>3</sub> a born figure-of-merit (FOM) as excellent potential material for APDs. However, so far the breakdown electric field of reported Ga<sub>2</sub>O<sub>3</sub>-based APDs is limited by the barrier height of the rectifying junction, which is much less than the often quoted theoretical breakdown field of Ga<sub>2</sub>O<sub>3</sub>. Very recently, we constructed an amorphous Ga<sub>2</sub>O<sub>3</sub>/ITO APDs with enlarged barrier height ( $\sim 2.07$  eV), resulting in dramatically improved reverse bias voltage and photoresponse<sup>21</sup>. Herein, the enlarged  $\Delta E_C$  between MgO and Nb:STO is further estimated up to 4.18 eV, promising larger tolerance of higher reverse bias. Next, we consider the distinctive role of unipolar barrier design influencing the avalanche progress under working condition (Fig. 2c). Note that owing to the electron concentration in Nb:STO ( $\sim 10^{20}$  cm<sup>-3</sup>) is much larger than that in unintentional doped Ga<sub>2</sub>O<sub>3</sub> ( $10^{16}$ - $10^{17}$  cm<sup>-3</sup>), the depletion region is mainly in Ga<sub>2</sub>O<sub>3</sub> side. Under UV light irradiation, charger carriers are acceleraed under high electric fields and hence more electron-hole pairs are ionized (Fig. 2d). Under avalanche breakdown, the extensive electrons are swept to the anode, while a negligible  $\Delta E_V$  across the heterojunctions facilitates the generated holes flowing unimpeded. The ideal APDs should separate electrons and holes as efficiently as possible, with minimal relaxation of charge carriers from the avalanche multiplication. Unipolar barrier construction filters out photocurrent components on demand, rather than aggregating them at the interfaces, which can reduce the adverse recombination rate. Furthermore, the holes aggregation would give rise to an electric field counteracts the externally applied field, and impair the avalanche process.

**Unipolar barrier APDs.** Figure 3a schematically presents the device of Ga<sub>2</sub>O<sub>3</sub>/MgO/Nb:STO nBn unipolar barrier APD and Ga<sub>2</sub>O<sub>3</sub>/Nb:STO n-n isotype APD. As the nBn unipolar barrier heterostructure is designed to suppress dark current and enhance avalanche gain, carrier transport behaviors in dark were first investigated, as shown in Fig. 3b. To prevent unrecoverable breakdown in both APDs, 5  $\mu$ A corresponding to 500  $\mu$ A/mm<sup>2</sup> is set as the limit current. Obvious rectifying behaviors are observed in the current-voltage ( $I$ - $V$ ) curves of both two types of heterostructures. Consistent with the proposed transport mechanism as discussed above, the dark current in the nBn unipolar barrier heterostructure is much smaller than that in the n-n isotype heterostructure, especially under a reverse bias. Note that the dark current in the Ga<sub>2</sub>O<sub>3</sub>/MgO/Nb:STO heterostructure remained below 0.06 nA (0.006  $\mu$ A/mm<sup>2</sup>) under 50 V reverse bias, where the dark current in the Ga<sub>2</sub>O<sub>3</sub>/Nb:STO already reached 5  $\mu$ A (500  $\mu$ A/mm<sup>2</sup>). Thus, the large conduction band barrier exhibits significant inhibition of dark current over more than one order of magnitude, which provides great advantages for improving the internal gain and detectivity of APD. Figure 3c

demonstrates the dark current and photocurrent (under  $0.1 \mu\text{W}/\text{cm}^2$  254 nm light irradiation), as well as the calculated gain versus reverse voltage for the two types of APDs. Here, the unmultiplied current at 1 V was assigned as the unity gain reference. It is found that the avalanche breakdown threshold voltages (calculated onset avalanche electric fields) are 31 V (1.55 MV/cm) and 71 V (3.16 MV/cm) for the  $\text{Ga}_2\text{O}_3/\text{Nb}:\text{STO}$  and the  $\text{Ga}_2\text{O}_3/\text{MgO}/\text{Nb}:\text{STO}$  heterostructures, respectively. The avalanche gain ( $M$ ) is determined using the following relation:  $M = [I_{ph}(V) - I_d(V)] / [I_{ph}(0) - I_d(0)]$ , where  $I_{ph}(V)$  and  $I_d(V)$  are the multiplied photocurrent and dark current, whereas  $I_{ph}(0)$  and  $I_d(0)$  are the unmultiplied photocurrent and dark current, respectively<sup>23</sup>. With increasing the reverse voltage, the avalanche gain values keep increase exponentially, as shown in Fig. 3c (right axis). Compared to the maximum  $M$  value of  $5.30 \times 10^4$  at 43.6 V (2.18 MV/cm) in the  $\text{Ga}_2\text{O}_3/\text{Nb}:\text{STO}$  n-n isotype APD, the maximum  $M$  value for the  $\text{Ga}_2\text{O}_3/\text{MgO}/\text{Nb}:\text{STO}$  nBn unipolar barrier APD increased by one order of magnitude and reaches as high as  $5.86 \times 10^5$  at 78.1 V (3.47 MV/cm), which is the record-high avalanche gain value reported in  $\text{Ga}_2\text{O}_3$ -based solar-blind APDs. Graphically, the “performance squaresee” defined by three key parameters of APD including dark current, reverse workind voltage and gain is significantly amplified for unipolar barrier APD. Thus, order of magnitude improvements in both dark current and gain fullfill our unipolar barrier design intention. Temperature dependent threshold voltages investigation presents a positive temperature coefficient of  $0.026 \text{ V}/^\circ\text{C}$ , indicating that the underly mechanism of the breakdown is attributed to avlanche effect instead of Zener tunneling effect (Supplementary Fig. S5). To access the ultraweak light detection ability of the APD device, several critical FOMs, specific detectivity ( $D^*$ ) and linear dynamic range (LDR) were later quantitatively evaluated using the following equations:  $D^* = RS^{1/2}/(2eI_d)^{1/2}$  and  $\text{LDR} = 20 \times \log(I_{ph}/I_d)$ , respectively<sup>31,32</sup>. Here,  $R$  represents the responsivity<sup>21</sup>, which could be calculated by  $R = (I_{ph} - I_d)/(P \times S)$ .  $P$ ,  $S$  and  $e$  represent incident light intensity, effective irradiation area and electron charge, respectively. As displayed in Fig. 3d, the maximum  $D^*$  increases from  $1.22 \times 10^{16}$  Jones to  $3.28 \times 10^{17}$  Jones, and the maximum LDR increases from 21.7 dB to 81.8 dB for  $\text{Ga}_2\text{O}_3/\text{Nb}:\text{STO}$  and  $\text{Ga}_2\text{O}_3/\text{MgO}/\text{Nb}:\text{STO}$  heterostructures, respectively. The enhancement of  $D^*$  and LDR values indicate that the MgO layer introduced through deliberate lattice and band engineering play a major role in the  $\text{Ga}_2\text{O}_3/\text{MgO}/\text{Nb}:\text{STO}$  nBn unipolar barrier APDs, leading to excellent ultraweak light detection with low noise and linear responsivity for a wide range of light intensities<sup>32</sup>.

The detailed photoresponse performance of the  $\text{Ga}_2\text{O}_3/\text{MgO}/\text{Nb}:\text{STO}$  nBn unipolar barrier APD was then systematically investigated. Figure 4a displays the  $I$ - $V$  curves of the device measured under different light intensity under reverse bias, all revealing outstanding photoresponse behaviors. The  $R$  and  $D^*$  as functions of light intensities and applied bias are presented in Fig. 4b and Fig. 4c, respectively. It is found that with an increase in light intensity, both  $R$  and  $D^*$  of the device decrease, which could be explained by the increased probability of electron-hole recombination under high intensity light illumination. The responsivity can reach up to  $4.46 \times 10^5 \text{ A}/\text{W}$  under  $0.1 \mu\text{W}/\text{cm}^2$  light irradiation at -78.1 V, which is among the best performance of  $\text{Ga}_2\text{O}_3$ -based solar-blind photodetectors<sup>2,6,12</sup>. The photoresponse performance of the  $\text{Ga}_2\text{O}_3/\text{Nb}:\text{STO}$  n-n isotype APD was also studied for comparison (Supplementary Fig. S6-S8). The spectral response of the device in the range of 200–700 nm was studied, as shown in Fig. 4d. The responsivity reaches its maximum value at  $\sim 260 \text{ nm}$  with a cutoff edge at  $\sim 280 \text{ nm}$ , revealing an excellent solar-blind region spectral selectivity. Response speed is another important parameter for the APD. To assess the temporal response speed of the APD, the transient photoresponse signal was measured using a coherent KrF 248 nm pulse laser combined with a 500 MHz oscilloscope, as depicted in Fig. 4e. By fitting the transient response curves using  $I = I_0 + A_1 e^{-t/\tau_1} + A_2 e^{-t/\tau_2}$  Eq. 6, the obtained rise/decay time  $\tau_r/\tau_d$  are 12.4 ns and 41.7  $\mu\text{s}$ , respectively. So fast response speed could be understood by the rapid electron-hole separation and transport owing to the enhanced avalanche electric fields and dispelling holes at the interface. The stability and reliability of the nBn unipolar barrier APD were further examined by periodic turn on/off the UV lamp. As displayed in Fig. 4f, the APD retained reliable photoresponse characteristics even after  $10^4$  on/off cycles.

### 3. Discussion

We have shown that key parameters of  $\text{Ga}_2\text{O}_3$ -based solar blind APDs including gain and detectivity can be greatly enhanced through a deliberated lattice and band engineered unipolar barrier design. Ga atoms in the  $\beta\text{-Ga}_2\text{O}_3$  (100) plane bonding to the oxygen atom in the MgO (100) plane with  $45^\circ$  in-plane rotation significantly alleviates the large lattice mismatch between them.

The nBn heterostructure with subtle selection of insulate dielectric MgO exhibits large conduction band offset and near zero valence band offset. The deterministic configuration of the nBn unipolar barrier profile provides desired control over the charge carriers flow and related avalanche multiplication effects. High dark currents are the primary contributor to noise and inherently limits the detectivity and gain in APDs. The enlarged conduction band barrier exhibits significant suppression of dark current over more than one order of magnitude. Moreover, the breakdown field predicted for the APD is determined by the rectifying junction with the barrier height. We have investigated the band alignment of Ga<sub>2</sub>O<sub>3</sub>/MgO/Nb:STO heterojunction with  $\Delta E_C$  estimated up to 3.01 eV and 4.18 eV, which allows a maximum breakdown field (3.47 MV/cm) among all reported Ga<sub>2</sub>O<sub>3</sub>-based APDs, giving rise to a record-high avalanche gain value  $5.86 \times 10^5$  (at 78.1 V). In our case, the nBn unipolar barrier blocks majority electron carriers and allows unimpeded flow of holes. Compared with bipolar barrier heterostructure, it reduces the recombination rate and facilitates the separation and transport of electrons and holes, leading to unprecedented APD characteristics including gain, detectivity and response speed. Main parameters for PDs are summarized in Supplementary **Table 1**, the responsivity and detectivity *versus* avalanche gain are also shown in Fig. 5a<sup>20-22, 33-39</sup>. It is obvious that our developed APD demonstrates a record-high gain and FOMs according to its performance metrics, which is even comparable to commercial PMT. The comparison of PMT and nBn unipolar barrier APD in terms of size, construction, and integration compatible was also demonstrated in Fig. 5b<sup>39,40</sup>. More importantly, since Ga<sub>2</sub>O<sub>3</sub> is emerging as key building block for various applications of power electronics and new-generation optoelectronics, the tunable rectifying characteristics plus the integrating capability with dielectrics in this work offer exciting opportunities to build Ga<sub>2</sub>O<sub>3</sub>-based electronic and optoelectronic devices with dramatically improved performance.

## 4. Methods

**Film Growth and Device Fabrication:** Commercial 10×10 mm<sup>2</sup> (001)-oriented 0.05 wt% Nb-doped SrTiO<sub>3</sub> (Nb:STO) single crystals (KJMTI) with a typical resistivity of 0.07 Ω·cm were purchased as the substrates. 100×100 μm<sup>2</sup> squared patterns were defined on the surface of Nb:STO substrates via standard photolithography, followed by a subsequent amorphous SrTiO<sub>3</sub> deposition as hard mask and lift-off process. Next, 25 nm thick MgO barrier layer was grown on the Nb:STO substrate using laser molecular beam epitaxy (KrF 248 nm) with the following fabrication parameters: laser energy of 1.2 J/cm<sup>2</sup>, pulse repetition rate of 1 Hz, substrate temperature of 700°C and O<sub>2</sub> pressure of 1×10<sup>-2</sup> Pa. 200 nm thick Ga<sub>2</sub>O<sub>3</sub> film was subsequently grown on the MgO layer with the following fabrication parameters: laser energy of 0.8 J/cm<sup>2</sup>, pulse repetition rate of 2 Hz, substrate temperature of 750°C and O<sub>2</sub> pressure of 1 Pa. A Ga<sub>2</sub>O<sub>3</sub>/Nb:STO sample (without MgO barrier layer) was also fabricated using the same parameter as a comparison. During the deposition, the growth of heterostructures was monitored *in-situ* by RHEED to ensure precise atomic-level growth. After the growth, all samples were *in situ* annealed in 200 mbar O<sub>2</sub> at 470°C for 30 min, before the final cooling down to room temperature. 30×30 μm<sup>2</sup> squared Au/Ti electrodes (30 nm/20 nm) and gold pads (100 nm) were fabricated by sputtering on the top Ga<sub>2</sub>O<sub>3</sub> layer and back side of the Nb:STO substrate respectively to form Ohmic contacts.

**Material Characterizations and Photoresponse Measurements:** X-ray diffractometer (Bruker D8 Discover: λ = 1.5406 Å, Cu Kα1 radiation) was employed to investigate the crystal structure of the samples. A Bruker DI3 Atomic Force Microscope (AFM) was used to characterize the surface morphology of the samples. The X-ray photoelectron spectroscopy (XPS) measurements were taken using a ThermoFisher Scientific ESCALAB 250Xi instrument. The photoresponse *I*-*V* curves under varying irradiation intensities at the wavelength of 254 nm were recorded by a Keithly-4200 SCS semiconductor analyzer connected to a probe station using triaxial cables to ensure low-noise measurements.

**Energy band alignments of the Ga<sub>2</sub>O<sub>3</sub>/MgO/Nb:STO heterostructure:** XPS scan was used to quantitatively determine the energy band alignments of the nBn heterostructure. Four samples: Nb:STO substrate, MgO (100 nm)/Nb:STO, Ga<sub>2</sub>O<sub>3</sub> (200 nm)/MgO (25 nm)/Nb:STO, and ultrathin Ga<sub>2</sub>O<sub>3</sub> (3 nm)/MgO (2 nm)/Nb:STO were fabricated using the same growth condition described in *Film Growth and Device Fabrication* section. Kraut's method was employed to calculate the valence band offset ( $\Delta E_V$ ) and conduction band offset ( $\Delta E_C$ ) by using the following equations:

$$\Delta E_{V-Ga_2O_3/MgO} = \left( E_{Ga-core}^{Ga_2O_3} - E_{VBM}^{Ga_2O_3} \right) - \left( E_{Mg-core}^{MgO} - E_{VBM}^{MgO} \right) - \left( E_{Ga-core}^{Ga_2O_3/MgO/Nb:STO} - E_{Mg-core}^{Ga_2O_3/MgO/Nb:STO} \right)$$

$$\Delta E_{V-MgO/Nb:STO} = \left( E_{Mg-core}^{MgO} - E_{VBM}^{MgO} \right) - \left( E_{Ti-core}^{Nb:STO} - E_{VBM}^{Nb:STO} \right) - \left( E_{Mg-core}^{Ga_2O_3/MgO/Nb:STO} - E_{Ti-core}^{Ga_2O_3/MgO/Nb:STO} \right)$$

where  $E_{Ga-core}^{Ga_2O_3}$ ,  $E_{Mg-core}^{MgO}$ ,  $E_{Ti-core}^{Nb:STO}$ ,  $E_{VBM}^{MgO}$ ,  $E_{VBM}^{Ga_2O_3}$ , and  $E_{VBM}^{Nb:STO}$  are the core levels of Ga 2p, Mg 2p, Ti 2p, and binding energy of the VBM for Ga<sub>2</sub>O<sub>3</sub> (200 nm)/MgO (25 nm)/Nb:STO sample, MgO (100 nm)/Nb:STO sample and Nb:STO substrate, respectively. Therefore, the obtained  $\Delta E_V$  for Ga<sub>2</sub>O<sub>3</sub>/MgO and MgO/Nb:STO are 0.12 eV and 0.45 eV, respectively. Given the respective bandgaps ( $E_g$ ) for  $\beta$ -Ga<sub>2</sub>O<sub>3</sub> (4.94 eV), MgO (7.83 eV), and Nb:STO (3.2 eV), the conduction band minimum (CBM) for the heterostructure could be consequently determined. And the obtained values of  $\Delta E_C$  for Ga<sub>2</sub>O<sub>3</sub>/MgO and MgO/Nb:STO are 3.01 eV and 4.18 eV, respectively. The negligible  $\Delta E_V$  and extremely large  $\Delta E_C$  values for Ga<sub>2</sub>O<sub>3</sub>/MgO/Nb:STO indicate that an nBn unipolar barrier heterostructure is formed.

## Declarations

### Data availability

The data that support the findings of this study are available from the corresponding authors upon reasonable request.

### Acknowledgements

This work was supported by the National Natural Science Foundation of China (No. 12074044, 11874230), the Fund of State Key Laboratory of Information Photonics and Optical Communications (IPOC2021ZT05), Natural Science Foundation of Tianjin (18JCYBJC41500), and the Fundamental Research Funds for the Central Universities (BUPT).

### Author Contributions

Z.W., Y.Z., and J.H. designed the project and analyzed the data. Q.Z. and N.L. produced the sample and executed the experiments. Q.Z., N.L., Y.Y., Z.D., J.S. and T.Z., completed the microstructure measurements. Q.Z., T.Z., Y.W., D.D. and Y.L. conducted the XPS characterizations. Q.Z., N.L., Y.Y. and W.T. carried out photoresponse measurements. Z.W., Y.Z. and J.H. wrote the paper with contributions of all authors.

### Competing interests

The authors declare no competing interest.

### Additional information

Supplementary Information is available for this paper.

**Correspondence and requests for materials** should be addressed to Y. Z., Z.W. or J.H.

## References

1. Cai, Q. *et al.* Progress on AlGaIn-based solar-blind ultraviolet photodetectors and focal plane arrays. *Light Sci. Appl.* **10**, 94, (2021).
2. Kaur, D. & Kumar, M. A strategic review on gallium oxide based deep-ultraviolet photodetectors: Recent progress and future prospects. *Adv. Opt. Mater.* **9**, 2002160, (2021).
3. Chen, J., Ouyang, W., Yang, W., He, J.-H. & Fang, X. Recent progress of heterojunction ultraviolet photodetectors: Materials, integrations, and applications. *Adv. Funct. Mater.* **30**, 1909909, (2020).
4. Xu, Z. & Sadler, B. M. Ultraviolet communications: Potential and state-of-the-art. *IEEE Commun. Mag.* **46**, 67–73, (2008).
5. Hadfield, R. H. Single-photon detectors for optical quantum information applications. *Nat. Photonics* **3**, 696–705, (2009).

6. Xu, J., Zheng, W. & Huang, F. Gallium oxide solar-blind ultraviolet photodetectors: A review. *J. Mater. Chem. C* **7**, 8753–8770, (2019).
7. Wang, D. *et al.* Bidirectional photocurrent in p–n heterojunction nanowires. *Nat. Electron.* **4**, 645–652, (2021).
8. Xie, C. *et al.* Recent progress in solar-blind deep-ultraviolet photodetectors based on inorganic ultrawide bandgap semiconductors. *Adv. Funct. Mater.* **29**, 1806006, (2019).
9. Li, D., Jiang, K., Sun, X. & Guo, C. AlGaIn photonics: Recent advances in materials and ultraviolet devices. *Adv. Opt. Photonics* **10**, 43–110, (2018).
10. Du, X. *et al.* Controlled growth of high-quality ZnO-based films and fabrication of visible-blind and solar-blind ultra-violet detectors. *Adv. Mater.* **21**, 4625–4630, (2009).
11. Pearton, S. J. *et al.* A review of Ga<sub>2</sub>O<sub>3</sub> materials, processing, and devices. *Appl. Phys. Rev.* **5**, 011301, (2018).
12. Yuan, Y. *et al.* Toward emerging gallium oxide semiconductors: A roadmap. *Fundam. res.* **1**, 697–716, (2021).
13. Chen, X., Ren, F., Gu, S. & Ye, J. Review of gallium-oxide-based solar-blind ultraviolet photodetectors. *Photon. Res.* **7**, 381–415, (2019).
14. Kim, S., Oh, S. & Kim, J. Ultrahigh deep-UV sensitivity in graphene-gated β-Ga<sub>2</sub>O<sub>3</sub> phototransistors. *ACS Photonics* **6**, 1026–1032, (2019).
15. Hou, X. *et al.* High-performance harsh-environment-resistant GaO<sub>x</sub> solar-blind photodetectors via defect and doping engineering. *Adv. Mater.* **34**, 2106923, (2022).
16. Liu, N. *et al.* Fast-response amorphous Ga<sub>2</sub>O<sub>3</sub> solar-blind ultraviolet photodetectors tuned by a polar AlN template. *IEEE Electron Device Lett.* **43**, 68–71, (2022).
17. Chen, Y. *et al.* 3d solar-blind Ga<sub>2</sub>O<sub>3</sub> photodetector array realized via origami method. *Adv. Funct. Mater.* **29**, 1906040, (2019).
18. Qiao, B. *et al.* Avalanche gain in metal-semiconductor-metal Ga<sub>2</sub>O<sub>3</sub> solar-blind photodiodes. *J. Phys. Chem. C* **123**, 18516–18520, (2019).
19. Kong, W.-Y. *et al.* Graphene-β-Ga<sub>2</sub>O<sub>3</sub> heterojunction for highly sensitive deep UV photodetector application. *Adv. Mater.* **28**, 10725–10731, (2016).
20. Zhao, B. *et al.* Solar-blind avalanche photodetector based on single ZnO-Ga<sub>2</sub>O<sub>3</sub> core-shell microwire. *Nano Lett* **15**, 3988–3993, (2015).
21. Wang, Y. *et al.* Ultrahigh gain solar blind avalanche photodetector using an amorphous Ga<sub>2</sub>O<sub>3</sub>-based heterojunction. *ACS Nano* **15**, 16654–16663, (2021).
22. Chen, X. *et al.* Solar-blind photodetector with high avalanche gains and bias-tunable detecting functionality based on metastable phase α-Ga<sub>2</sub>O<sub>3</sub>/ZnO isotype heterostructures. *ACS Appl. Mater. Interfaces* **9**, 36997–37005, (2017).
23. Hayden, O., Agarwal, R. & Lieber, C. M. Nanoscale avalanche photodiodes for highly sensitive and spatially resolved photon detection. *Nat. Mater.* **5**, 352–356, (2006).
24. Chen, Y. *et al.* Unipolar barrier photodetectors based on van der Waals heterostructures. *Nat. Electron.* **4**, 357–363, (2021).
25. Jagtap, A. *et al.* Design of a unipolar barrier for a nanocrystal-based short-wave infrared photodiode. *ACS Photonics* **5**, 4569–4576, (2018).
26. Bullock, J. *et al.* Polarization-resolved black phosphorus/molybdenum disulfide mid-wave infrared photodiodes with high detectivity at room temperature. *Nat. Photonics* **12**, 601–607, (2018).
27. Akhavan, N. D., Umana-Membreno, G. A., Gu, R., Antoszewski, J. & Faraone, L. Delta doping in HgCdTe-based unipolar barrier photodetectors. *IEEE Trans. Electron Devices* **65**, 4340–4345, (2018).
28. Liu, Z. *et al.* Band alignments of β-Ga<sub>2</sub>O<sub>3</sub> with MgO, Al<sub>2</sub>O<sub>3</sub> and MgAl<sub>2</sub>O<sub>4</sub> measured by x-ray photoelectron spectroscopy. *J. Phys. D: Appl. Phys* **52**, 295104, (2019).
29. Zhang, J., Shi, J., Qi, D.-C., Chen, L. & Zhang, K. H. L. Recent progress on the electronic structure, defect, and doping properties of Ga<sub>2</sub>O<sub>3</sub>. *APL Mater.* **8**, 020906, (2020).

30. Greczynski, G. & Hultman, L. X-ray photoelectron spectroscopy: Towards reliable binding energy referencing. *Prog. Mater. Sci.* **107**, 100591, (2020).
31. Guo, D. *et al.* Self-powered ultraviolet photodetector with superhigh photoresponsivity (3.05 A/W) based on the GaN/Sn:Ga<sub>2</sub>O<sub>3</sub> pn junction. *ACS Nano* **12**, 12827–12835, (2018).
32. García de Arquer, F. P., Armin, A., Meredith, P. & Sargent, E. H. Solution-processed semiconductors for next-generation photodetectors. *Nat. Rev. Mater.* **2**, 16100, (2017).
33. Mahmoud, W. E. Solar blind avalanche photodetector based on the cation exchange growth of  $\beta$ -Ga<sub>2</sub>O<sub>3</sub>/SnO<sub>2</sub> bilayer heterostructure thin film. *Sol. Energy Mater. Sol. Cells* **152**, 65–72, (2016).
34. Li, Z. *et al.* High-performance  $\beta$ -Ga<sub>2</sub>O<sub>3</sub> solar-blind schottky barrier photodiode with record detectivity and ultrahigh gain via carrier multiplication process. *IEEE Electron Device Lett.* **41**, 1794–1797, (2020).
35. Wu, H. *et al.* All AlGaN epitaxial structure solar-blind avalanche photodiodes with high efficiency and high gain. *Appl. Phys. Express* **9**, 052103, (2016).
36. Sun, L., Chen, J., Li, J. & Jiang, H. AlGaN solar-blind avalanche photodiodes with high multiplication gain. *Appl. Phys. Lett.* **97**, 191103, (2010).
37. Tut, T., Gokkavas, M., Inal, A. & Ozbay, E. Al<sub>x</sub>Ga<sub>1-x</sub>N-based avalanche photodiodes with high reproducible avalanche gain. *Appl. Phys. Lett.* **90**, 163506, (2007).
38. Huang, Z., Li, J., Zhang, W. & Jiang, H. AlGaN solar-blind avalanche photodiodes with enhanced multiplication gain using back-illuminated structure. *Appl. Phys. Express* **6**, 054101, (2013).
39. *Photomultiplier tube products from Hamamatsu Photonics*, <[www.hamamatsu.com/us/en/product/optical-sensors/pmt/pmt\\_tube-alone/head-on-type.html](http://www.hamamatsu.com/us/en/product/optical-sensors/pmt/pmt_tube-alone/head-on-type.html)> (2022).
40. Photonics, H. *Photomultiplier tubes*. (Hamamatsu, 2000).

## Figures

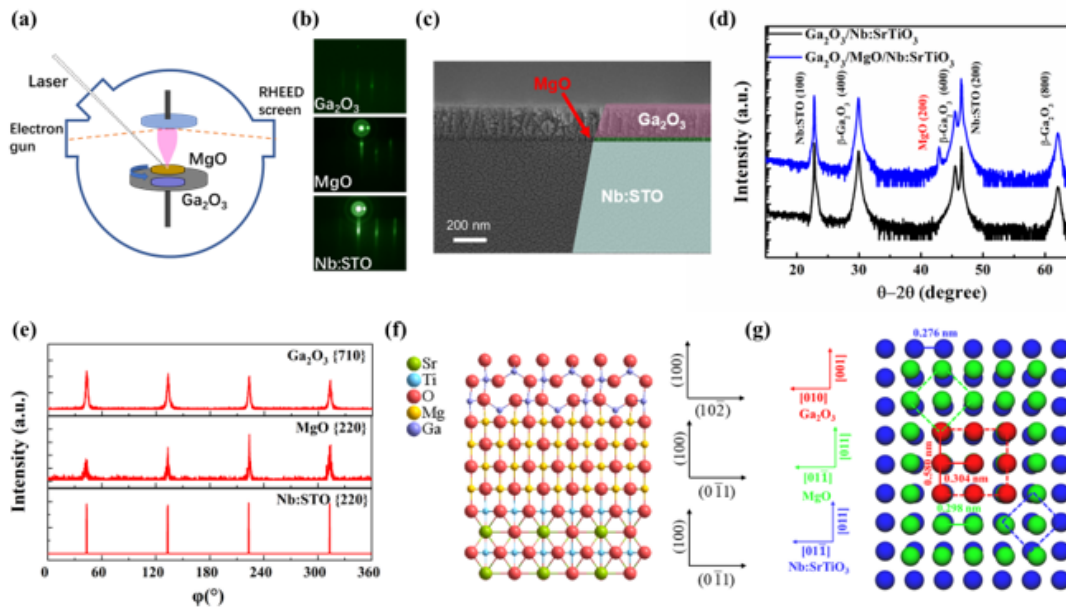


**Figure 1**

**Synthesis and structural characterizations of the nBn unipolar barrier heterostructure.** (a) Schematic process for heterostructure growth. (b) RHEED patterns of Ga<sub>2</sub>O<sub>3</sub>, MgO, and Nb:STO. (c) Cross-sectional SEM image. (d) XRD  $\theta$ - $2\theta$  scan. (e) XRD  $\Phi$ -scan. (f)

Schematic atomic arrangement of the cross-sectional heterostructure. (g) Schematic interfacial oxygen-atom arrangements.

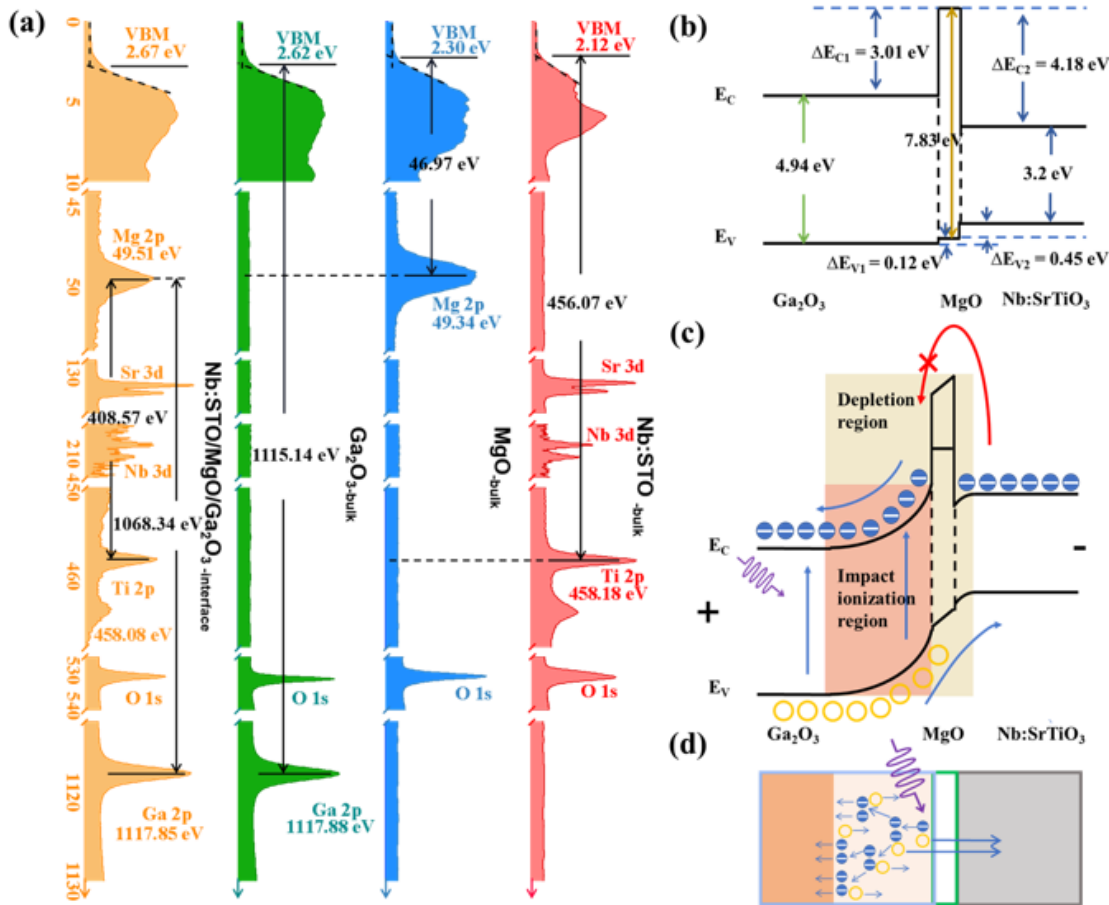


Figure 2

**XPS characterization and band diagrams of the nBn unipolar barrier heterostructure.** (a) Valence band spectra and the core-levels for the Nb:STO bulk, MgO bulk, Ga<sub>2</sub>O<sub>3</sub> bulk, and Ga<sub>2</sub>O<sub>3</sub>/MgO/Nb:STO interface. Band diagram of Ga<sub>2</sub>O<sub>3</sub>/MgO/Nb:STO heterostructure in equilibrium conditions (b) and in avalanche condition (c). (d) Illustration of the avalanche process in the nBn unipolar barrier APDs.

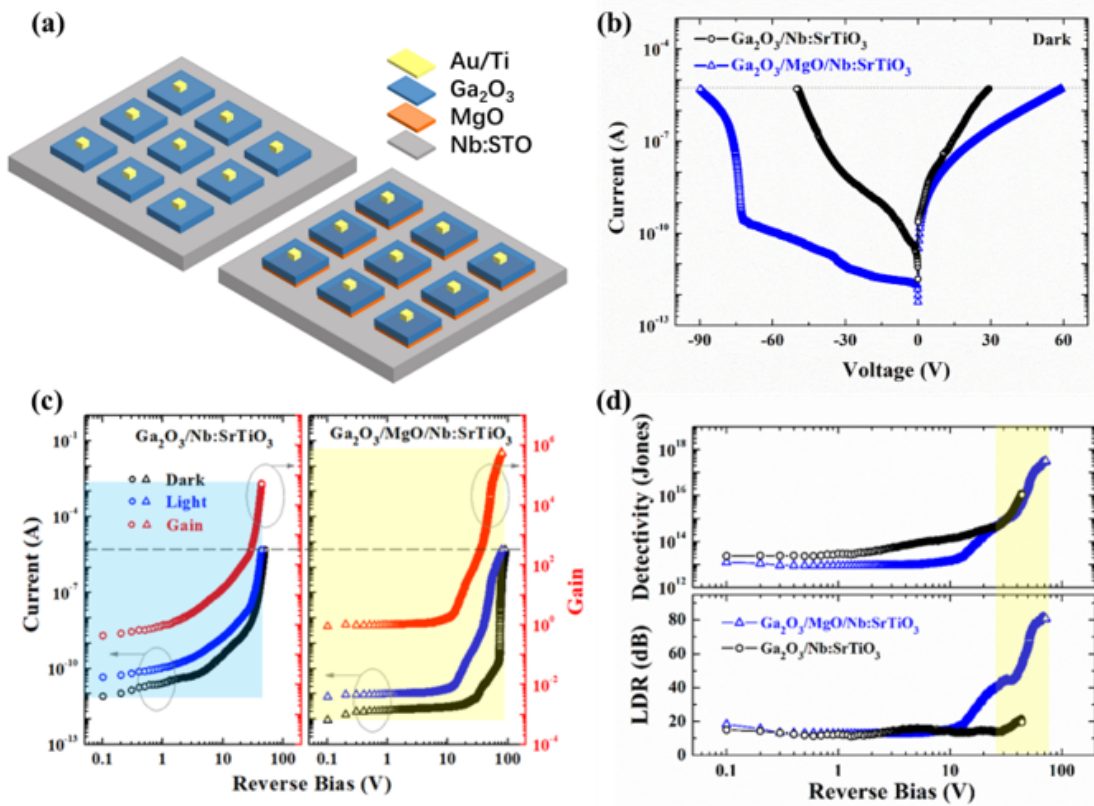


Figure 3

APDs performance comparison of the nBn unipolar barrier heterostructure and the n-n isotype heterostructure. (a) Schematic device illustrations of the Ga<sub>2</sub>O<sub>3</sub>/MgO/Nb:STO nBn unipolar barrier APD, and the Ga<sub>2</sub>O<sub>3</sub>/Nb:STO n-n isotype APD. (b) Current-voltage (*I-V*) characteristics of both devices. (c) Reverse *I-V* curves in dark and under UV illumination for both devices; the right axis illustrates the gain. (d) Detectivity and LDR as a function of reverse bias for both devices.

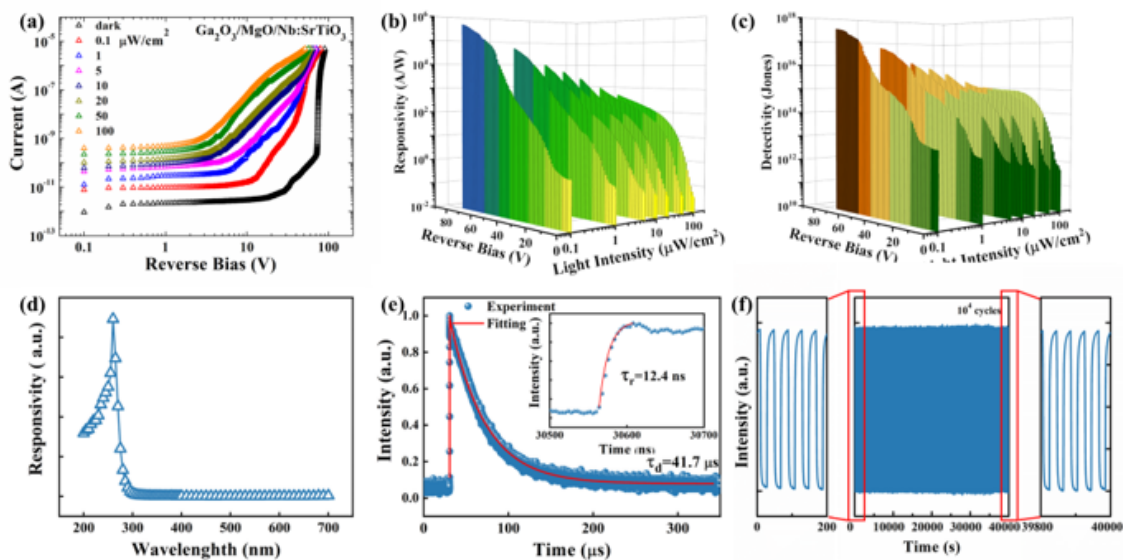


Figure 4

**Photoresponse characteristics the nBn unipolar barrier APD.** (a) Reverse  $I$ - $V$  characteristics of the nBn unipolar barrier APD in the dark and under various intensity 254 nm light illumination. The responsivity (b) and detectivity (c) as functions of light intensities and applied bias. (d) Wavelength-dependent responsivity under reverse bias. (e) Transient response curve of the device; the inset reveals the enlarged rise edge. (f) Stability and reliability characteristics of the nBn unipolar barrier APD after  $10^4$  light ON/OFF cycles.

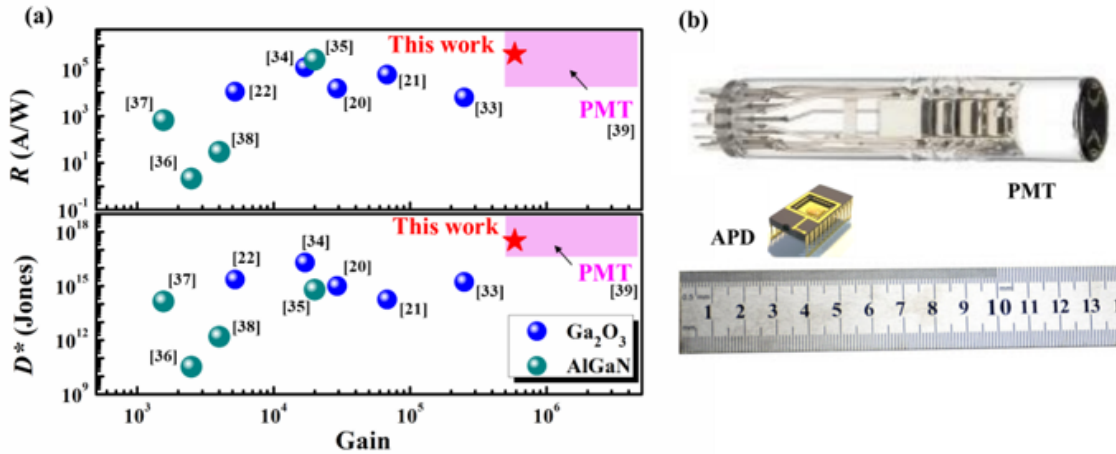


Figure 5

Performance comparison of the  $\text{Ga}_2\text{O}_3/\text{MgO}/\text{Nb:STO}$  nBn unipolar barrier APD with previous reported APDs and PMTs. (a) Responsivity and detectivity *versus* gain. (b) Comparison of PMT and nBn unipolar barrier APD in terms of size, construction, and integration compatible.

## Supplementary Files

This is a list of supplementary files associated with this preprint. Click to download.

- [UnipolarbarrierAPDSupportingInformation.docx](#)